

# Improving Spatial Resolution Using Incoherent Subtraction of Receive Beams Having Different Apodizations

Anil Agarwal<sup>1</sup>, Graduate Student Member, IEEE, Jonathan Reeg, Member, IEEE, Anthony S. Podkowa, Graduate Student Member, IEEE, and Michael L. Oelze<sup>2</sup>, Senior Member, IEEE

**Abstract**—In ultrasonic imaging, reduction of lateral sidelobes can result in an improved image with less distortion and fewer artifacts. In general, apodization is used to lower sidelobes in exchange for increasing the width of the main lobe, and thus decreasing lateral resolution. Null subtraction imaging (NSI) is a nonlinear image processing technique that uses different receive apodizations on copies of the same RF data to maintain low sidelobe levels while simultaneously improving lateral resolution. The images created with three different apodization functions are combined to form an image with low sidelobe levels and apparent improvements in lateral resolution compared to conventional rectangular apodization. To evaluate the performance of this technique for different imaging tasks, experiments were performed on an AT5539 phantom containing wire targets to assess lateral resolution and cylindrical anechoic and hyperechoic targets to assess contrast. NSI images were compared against rectangular apodized images and minimum variance beamformed images. In experiments, the apparent lateral resolution was observed to improve by a factor of more than 35 $\times$  when compared to rectangular apodization. Image quality was assessed by the estimation of lateral resolution ( $-6$ -dB receive beamwidth), main-lobe-to-sidelobe ratio, and contrast-to-noise ratio (CNR). Imaging with NSI using a focal number of 2 ( $f/2$ ), the  $-6$ -dB beamwidth on receive as measured from a small wire target in the AT5 phantom was  $0.03\lambda$  compared to  $2.79\lambda$  for rectangular apodization. Sidelobes were observed to decrease by 32.9 dB with NSI compared to rectangular apodization. However, the ability to observe the contrast of anechoic and hyperechoic targets reduced when utilizing the NSI scheme, i.e., the CNR decreased from  $-3.05$  to  $-1.01$  for anechoic targets and  $1.65$  to  $0.45$  for the hyperechoic targets.

**Index Terms**—Apodization, beamforming, plane-wave imaging, ultrasound imaging.

## I. INTRODUCTION

**I**N MODERN medical ultrasonic imaging, backscattered echo data are captured by transducers, typically in the form

Manuscript received June 25, 2018; accepted October 9, 2018. Date of publication October 16, 2018; date of current version January 14, 2019. Research reported in this publication was supported by the National Institute of Biomedical Imaging and Bioengineering of the National Institutes of Health under award number R21EB020766. 5% of this research was financed by the award, and 95% was financed by nongovernmental sources. (Corresponding author: Michael L. Oelze.)

The authors are with the Beckman Institute for Advanced Science and Technology, University of Illinois at Urbana-Champaign, Urbana, IL 61801 USA, and also with the Department of Electrical and Computer Engineering, University of Illinois at Urbana-Champaign, Urbana, IL 61801 USA (e-mail: oelze@illinois.edu).

Digital Object Identifier 10.1109/TUFFC.2018.2876285

of an array of elements. These transducers send out pulses of ultrasound and then listen for echoes. In conventional B-mode imaging, the received signals composed from these echoes are beamformed, envelope detected, and then, the collective signals are stacked together to create the image. On both transmission and reception, weights may be assigned to the elements of a transducer array to shape its radiation pattern. This weighting is called apodization.

Apodization of the transducer elements is analogous to windowing a time-domain signal. Choosing a time-domain window function that reduces sidelobes in the frequency domain while still maintaining an optimal main lobe width is a classical problem in signal analysis. For most apodization schemes, reducing the sidelobes through apodization has the tradeoff of widening the main lobe [1]. Dolph [2] developed a weighting method, or apodization, using Chebyshev polynomials for a linear array antenna that shaped its radiation pattern such that the minimum main lobe width was achieved for a given maximum sidelobe level. This distribution function was then improved upon by Taylor in 1954 for the continuous line sources [3] resulting in tapered sidelobes located farther from the main lobe. Hoen [4] did a study applying nine different apodization schemes to a linear ultrasound array and studying their effects on the image quality, finding that four of these schemes (cosine, Hamming, sinc, and 10% truncated Gaussian) produced more desirable results than a rectangular weighted scheme.

More recently, Guenther and Walker [5], [6] developed apodization functions using a constrained least-squares implementation. In that work, apodization functions were created that reduced sidelobe levels below that of a Hamming apodization while maintaining the main lobe width. In another more recent approach, Seo and Yen [7] applied a dual apodization with cross-correlation scheme (DAX) to reduce clutter and sidelobe levels. Wang [8] developed an approach to select different sets of apodization functions to preserve the main lobe width and reduce sidelobe levels. In a more recent work, Guo *et al.* [9] attempted to improve the lateral resolution of ultrasonic images at different depths by implementing a dynamic apodization scheme. However, they did not improve lateral resolution over simple rectangular apodization. Sung and Jeong [10] introduced an apodization method that included multiple apodizations of the same data to achieve

sidelobe reduction while maintaining the main lobe width similar to rectangular apodization. In their simulation studies, they were able to suppress sidelobe levels by 9 dB while maintaining the main lobe width comparable to rectangular apodization. Most recently, He *et al.* [11] proposed a second-order comb algorithm to optimize weights and reduce sidelobes in near-field beamforming.

More recently, active research has been focused on adaptive beamforming techniques, which exploit local speckle statistics to optimally choose apodization weights [12]–[17]. These techniques are capable of significant improvements in lateral resolution in simulation, achieving as much as a factor of 10 improvement in lateral resolution [13]. However, such techniques are often computationally demanding, requiring  $O(M^3)$  computations compared to the  $O(M)$  computations required for classical delay and sum (DAS) beamforming, where  $M$  is the number of elements. To mitigate this additional computational cost while preserving some of the benefits of adaptive beamforming, a number of techniques have been proposed to address this issue. A low-complexity, data-dependent beamformer was introduced by Synnavag *et al.* [15]. This approach relied on reducing the set of possible apodization functions to  $P$  predefined apodization functions, thereby reducing the computational complexity to  $O(PM)$  with marginal degradation in resolution. However, such an approach highly depends on the choice of the predefined apodization functions, making the performance of such an approach difficult to generalize. Improvements in reconstruction time were also observed using a multibeam approach, by reusing a covariance matrix that only depended on the depth of the target [16]. This approach also demonstrated an increased robustness to noise and fewer free parameters compared to the traditional Capon beamformer.

The use of apodization has had a long history in shaping radiation patterns in diagnostic ultrasound imaging. Apodization techniques are used to trade the main lobe width for low sidelobes. Conversely, sidelobe levels can be traded for a narrower main lobe using parabolic weighting schemes. In this study, a new method of apodization is proposed that will markedly improve the apparent lateral resolution of the imaging system by a factor of more than  $35\times$  compared to rectangular apodization while simultaneously lowering sidelobe levels. The apodization scheme relies on using a null in the beam pattern to achieve imaging. Because the null of a beam can fall off faster than the roll off of the main lobe, spatial resolution can be improved over imaging with the main lobe, i.e., diffraction limits. Furthermore, the technique is computationally efficient. Apodization weights are precalculated and applied to the receive channels and not adjusted adaptively. In order to image with the beam nulls, a nonlinear processing scheme is employed.

## II. METHODS

The far-field beam pattern from an ultrasonic transducer or an array is related to the Fourier transform of the product of the aperture function and the apodization function [1]. For example, the beam pattern for a rectangular function is a sinc [see Fig. 1(a) and (c) (blue solid line)].

Based on these Fourier transform pairs, the beam pattern from an apodization function with a zero-mean weighting across the array results in a null occurring at broadside. Fig. 1(c) (red dashed line) shows a zero-mean apodization function's predicted beam pattern. The beam pattern for a rectangular window (no apodization) maintains a beamwidth limited by diffraction. However, if we compare the width of the rectangular apodization with one minus the zero-mean apodization beam pattern, the shape of the main beam falls off much faster for the “inverted” null beam. The property of the null beam can be exploited through a novel approach to improve the apparent lateral resolution while maintaining the low sidelobes.

In our implementation, received signals are acquired after using plane-wave imaging on transmit and are described in the following equation for an ideal scatterer [18, pp. 435], where  $V_R$  is the received voltage,  $A_{R,i}$  are the receive apodizations,  $V_T$  is the transmit voltage,  $R_f$  is the focus distance, and  $N$  is the number of transducer elements:

$$V_R(t) = \sum_{i=1}^N A_{R,i} V_T \left( t + \frac{2R_f}{c_0} \right). \quad (1)$$

Apodization is only used on receive such that the technique can be entirely implemented via postprocessing. Applying null subtraction imaging (NSI) apodizations on transmit would require three separate transmits. The first image is constructed using a zero-mean apodization on receive [see Fig. 1(b), blue line]. A second image is constructed by taking the zero-mean apodization and adding a small dc constant to the apodization, giving

$$A_{R1,i} = \begin{cases} 1 : & 1 \leq i < \frac{N}{2} \\ -1 : & \frac{N}{2} \leq i < N \end{cases} \quad (2)$$

$$A_{R2,i} = A_{R1,i} + c \quad (3)$$

where  $A_{R,i}$  is the receive apodization weight for element  $i$ ,  $N$  is the number of elements in the subaperture of the array, and  $c$  is the dc constant [see Fig. 1(b), red dashed line]. Because using this apodization would put more energy on one side of the beam pattern [see Fig. 1(d)], an image is formed using a third apodization constructed by mirroring the weights of the second apodization [see Fig. 1(b), yellow dashed line]. Note that it is not necessary to mirror the weights of the zero-mean apodization as it puts equal energy on both sides, and mirroring the weights produces an identical envelope image. These two dc offset apodized signals are beamformed, the envelope taken, and added together to produce a new image, henceforth called the dc sum image. The sum image is divided by two. This image is nearly equivalent to that of one taken with the zero-mean apodization, except for a “bridge” of small, positive nonzero values between the two main lobes of the null beam pattern. Fig. 2 shows the plots of the beam patterns with and without the “bridge” and the effect that different levels of dc bias have on the level of the “bridge.” The signals acquired using the zero-mean apodization are then beamformed and their envelope is taken. To create the

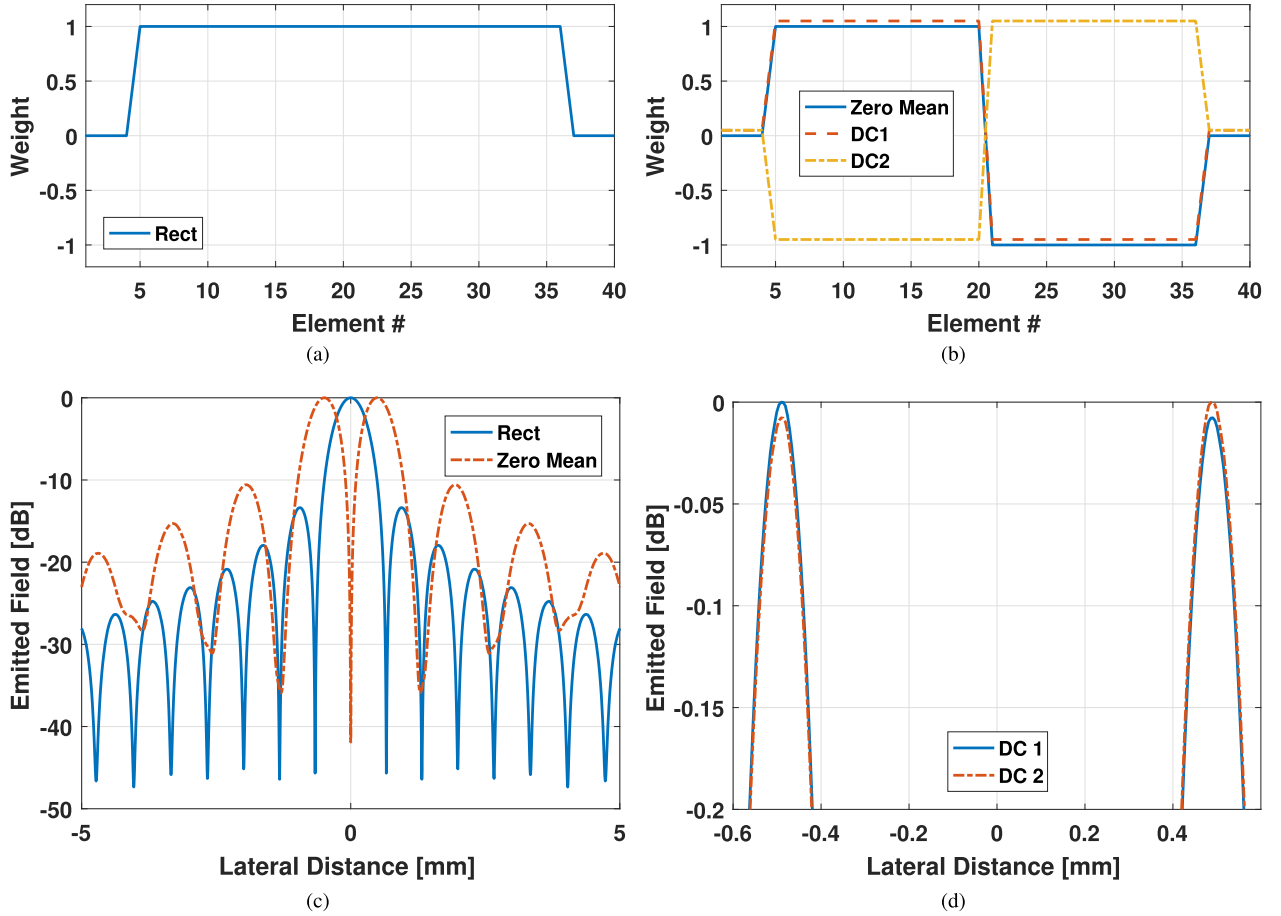


Fig. 1. Apodization functions and their associated beam patterns. (a) Rectangular apodization function where all 32 elements are weighted equally. (b) Blue solid line: zero-mean function where half of the elements are weighted equal in magnitude but with sign opposite to the other half. Red dashed line: zero-mean function with a dc constant of 0.05 added to all elements. Yellow dashed line: laterally flipped version of the red dashed function. (c) Solid blue line: beam pattern of a transducer with the weights defined in (a). Red dashed line: beam pattern of a transducer with the weights defined by the blue solid line in (b). (d) Beam patterns of the two “bridged” functions dc1 and dc2, showing the differences due to asymmetry.

NSI image, the zero-mean image is subtracted from the dc sum image, giving

$$E_{\text{NSI}} = \frac{E_{\text{DC1}} + E_{\text{DC2}}}{2} - E_{\text{ZM}} \quad (4)$$

where  $E_{\text{ZM}}$  represents the zero-mean envelope image,  $E_{\text{DC1}}$  and  $E_{\text{DC2}}$  represent the two dc offset envelope images, and  $E_{\text{NSI}}$  represents the final NSI image. The resulting envelope image is converted to a decibel scale with the maximum value normalized to zero and displayed in grayscale

$$E_{\text{NSI,dB}} = 20 \log_{10}(E_{\text{NSI}}) - \max[20 \log_{10}(E_{\text{NSI}})]. \quad (5)$$

Fig. 3 shows a block diagram representing the process of generating the NSI envelope from the raw RF data. Note that the three NSI apodizations are applied to the same frame of RF data, thus eliminating motion artifacts.

This approach bears resemblance to an approach used by Savoia *et al.* [19] except they used two transmits: a uniform apodization was used on transmit and receive followed by a zero-mean apodization on transmit and receive. The difference with NSI is that the apodizations ZM and DC1/DC2 are more similar to each other than the Rect and ZM as used in [19]. Therefore, NSI is able to achieve a much narrower beamwidth,

whereas the primary aim in [19] was to decrease sidelobe levels.

The beam pattern can be predicted for NSI by considering a simple array of  $N$  point elements with equal weight, which has a beam pattern given by

$$H(\theta) = \left| \frac{\sin\left(\frac{Nkd}{2} \sin(\theta)\right)}{N \sin\left(\frac{kd}{2} \sin(\theta)\right)} \right| \quad (6)$$

where  $d$  is the pitch of the array and  $k$  is the acoustic wavenumber. If half of the elements are weighted at  $+1$  and half at  $-1$ , the resulting zero mean beam pattern through direct summation and superposition is

$$H_{\text{ZM}}(\theta) = \left| \frac{2 \sin^2\left(\frac{Nkd}{4} \sin(\theta)\right)}{N \sin\left(\frac{kd}{2} \sin(\theta)\right)} \right|. \quad (7)$$

Therefore, the beam pattern when adding a small dc bias,  $c$ , to the weighting scheme is

$$H_{\text{DC}}(\theta) = \left| \frac{2 \sin^2\left(\frac{Nkd}{4} \sin(\theta)\right) + c \sin\left(\frac{Nkd}{2} \sin(\theta)\right)}{N \sin\left(\frac{kd}{2} \sin(\theta)\right)} \right|. \quad (8)$$

The beam pattern can then be estimated as

$$H_{\text{NSI}}(\theta) = H_{\text{DC}}(\theta) - H_{\text{ZM}}(\theta). \quad (9)$$

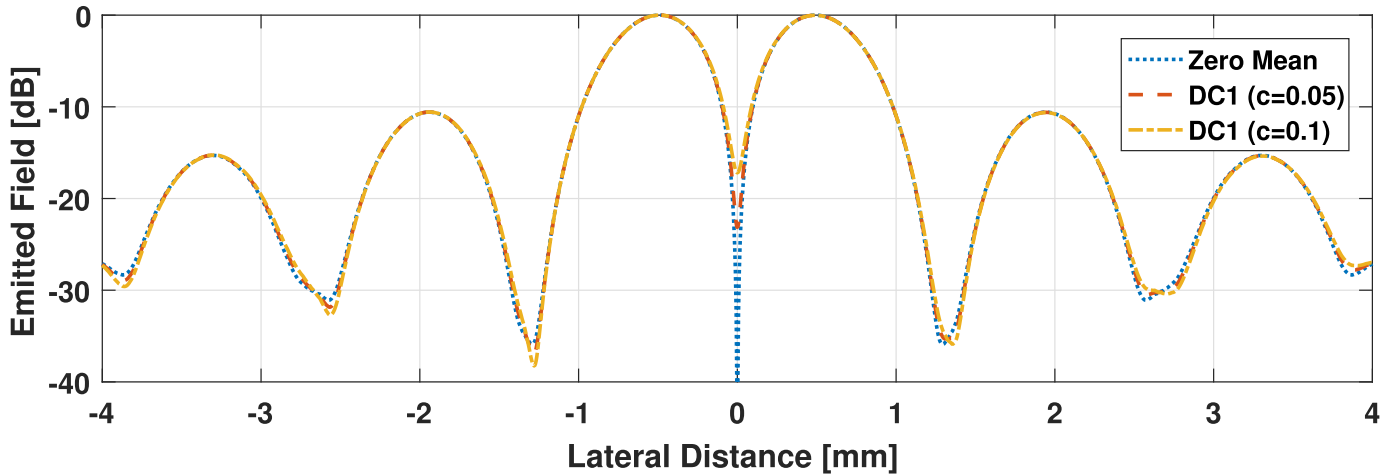


Fig. 2. Beam pattern of a transducer apodized with a zero-mean function (blue dotted line), a “bridged” function with  $c = 0.05$  (red dashed line), and a “bridged” function with  $c = 0.1$ .

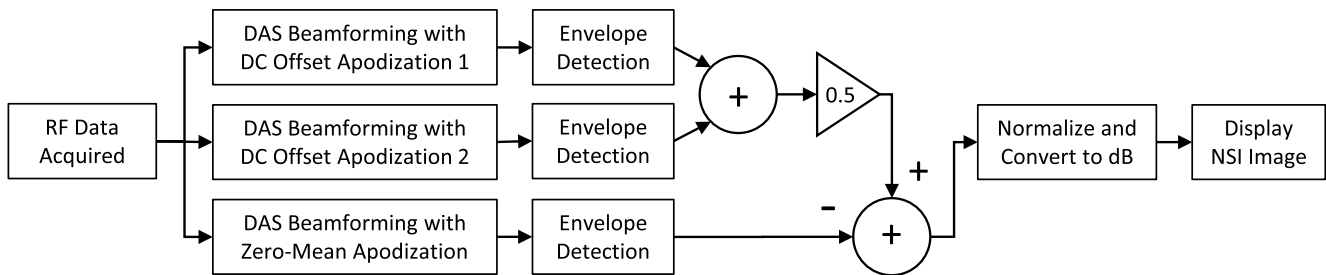


Fig. 3. Block diagram showing the process of generating an NSI image.

In the NSI apodization scheme, an adjustable parameter is the amount of dc bias applied to the apodization weights. By increasing the dc bias, the level of the “bridge” is increased. The level of the dc bias, therefore, affects the beamwidth and the main-lobe-to-sidelobe ratio (MSR). Equation (9) suggests that decreasing the dc bias results in a smaller beamwidth and a higher MSR. Equation (9) also indicates that increasing the number of elements,  $N$ , results in narrowing of the beamwidth.

### III. SIMULATIONS

Simulations were performed using Field II [20], [21] to quantify sidelobe levels associated with NSI compared to rectangular apodization. Simulations were conducted on a single point target located at the elevation focus of the simulated array to compare the utility of the NSI apodization approach to rectangular apodization. An L9-4/38 array transducer was simulated to match the physical experiments. The simulated array had 128 elements, with a pitch of 0.3048 mm, an element width of 0.2698 mm, an elevation focus of 19 mm, and a bandwidth of 3–7 MHz with a center frequency of 5 MHz. A plane wave was simulated in transmission. Beamforming on receive was conducted using simple DAS with 32-element subapertures of the array operating in a linear sequential scan mode. In order to increase the line density and obtain a smooth plot, the RF data were laterally upsampled by a factor of 8 using a 2-D spline interpolation prior to

TABLE I  
COMPARISON OF THE MSR FOR DIFFERENT APODIZATION SCHEMES

Depth	Rect	NSI ( $c = 0.05$ )	NSI ( $c = 0.1$ )	MV
19 mm	17.5 dB	50.4 dB	46.6 dB	65.6 dB

DAS beamforming. The sidelobe levels were estimated and the MSR was calculated in decibel for each apodization approach (see Table I). In addition, the dc bias was varied and values for beamwidth and MSR were recorded for different amounts of added noise.

Fig. 4 shows the simulated beam patterns for NSI, rectangular apodization, and minimum variance (MV) beamforming. It can be observed that the NSI beam pattern has a much narrower beamwidth compared to rectangular apodization, along with the characteristic “point” at the top of the main lobe given by “inverting” the null.

### IV. EXPERIMENTS

To assess the performance of the novel apodization scheme for conducting specific imaging tasks, imaging experiments were performed on an ATS539 phantom (ATS Laboratories, Norfolk, VA, USA) using an L9-4/38 clinical array transducer (measured center frequency of 5 MHz) with 128 elements and an Ultrasonix RP with a SonixDAQ. It is not possible to extract prebeamformed RF data from the Ultrasonix RP, as it performs

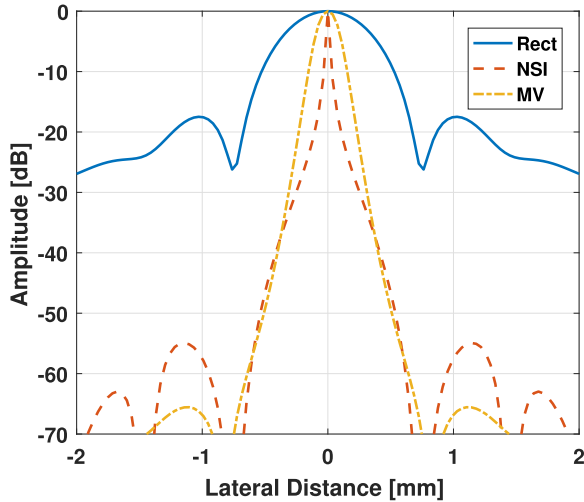


Fig. 4. Simulated beam patterns of the various apodization schemes.

DAS beamforming in its hardware before the signals are received by the system. The SonixDAQ was necessary to allow the collection of raw RF data that could be postprocessed using NSI. For all experiments, 5-MHz plane wave transmissions were used and the received RF was recorded from each of the 128 elements at a sampling frequency of 80 MHz.

#### A. Wire Target Experiments

Two experiments were performed using wire targets. In the first experiment, the ATS phantom's wire targets were scanned to analyze beam characteristics and the effect of added noise. Broadside plane-wave transmissions were used ( $\theta = 0^\circ$ ). As the results will show, the  $-6$ -dB beamwidth was often smaller than the line spacing for the linear sequential scan mode, where the separation between each line is equal to the pitch of the transducer array. For a single image with 128 scan lines, the minimum distance one can measure for the  $-6$ -dB beamwidth is the width of a scan line, which was not enough to accurately measure the  $-6$ -dB beamwidths of the targets. Therefore, to characterize the beamwidth of NSI more accurately, a finer lateral resolution was required. This was accomplished by first acquiring 128 scan lines, then physically moving the array laterally using a micropositioning system, in steps of  $5 \mu\text{m}$  to fill in additional sets of 128 scan lines, as shown in Fig. 5. At each position of the array, a new set of 128 scan lines was acquired. In total, to span the pitch of the array, the array was moved 61 times with the  $5\text{-}\mu\text{m}$  step size yielding 7808 scan lines in total per image frame.

In the second experiment, two closely spaced ( $<1$  mm) wire targets placed in a water tank were scanned to study the effects of the high lateral resolution. This setup was scanned with angular plane-wave transmissions where 41 angles equally spaced between  $\theta = -20^\circ$  and  $\theta = 20^\circ$  were used, and the RF data were laterally upsampled by a factor of 2 prior to beamforming.

#### B. Contrast Targets

The ATS phantom's anechoic and hyperechoic targets were scanned to study the effect of NSI on contrast. As it is not necessary to have a high sampling density for

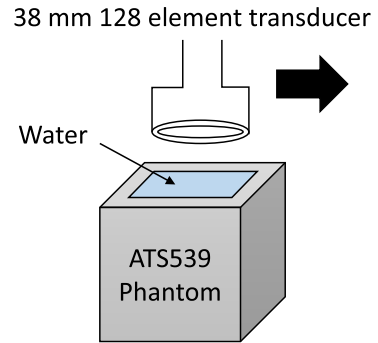


Fig. 5. Illustration of the experimental setup. The transducer scanned using plane-wave transmissions and was then translated physically in steps of  $5 \mu\text{m}$  to acquire additional sets of scan lines. This was repeated until a distance equal to the pitch of the array was spanned. The scan lines were interleaved to create an image with high scan line density.

contrast measurements, the transducer was not physically translated for these scans. The contrast targets were scanned using angular plane waves with 21 angles equally spaced between  $\theta = -20^\circ$  and  $\theta = 20^\circ$ .

#### C. Beamforming and Image Reconstruction

DAS beamforming with linear sequential scanning was used to reconstruct the images. A subaperture size of  $9.75$  mm was used for each beamformed scan line. This subaperture size corresponds to 1952 scan lines for the ATS phantom wire target scan and 32 scan lines for the other scans. Angular plane-wave scans were combined using coherent plane-wave compounding. NSI images were reconstructed using the apodizations described in Section II. The dc constant used for the wire target experiments was  $c = 0.01$ , and the dc constant used for the contrast experiments was  $c = 0.05$ .

In order to compare NSI with other beamforming techniques, images were also constructed using MV beamforming based on the procedure described in [22]. Due to the computational complexity of the MV beamformer, it was necessary to use a lower sampling density than that used for NSI and rectangular apodization in the wire target experiments. 1280 scan lines separated by  $30.4 \mu\text{m}$  were used, with a subaperture length of  $9.7$  mm (320 scan lines) to reconstruct the MV beamformed image.

A time gain compensation curve was applied to all envelope images based on the attenuation of the ATS539 phantom, i.e.,  $0.5 \text{ dB MHz}^{-1}\text{cm}^{-1}$ .

#### D. Evaluation Metrics

The ATS539 multipurpose phantom was used to quantify the technique for performing different imaging tasks, and to evaluate how the technique affected the contrast-to-noise ratio (CNR) of contrast targets (both hyperechoic and anechoic) in the phantom, with CNR defined as

$$\text{CNR} = \frac{\mu_{\text{in}} - \mu_{\text{out}}}{\sqrt{\sigma_{\text{in}}^2 + \sigma_{\text{out}}^2}} \quad (10)$$

where  $\mu_{\text{in}}$  is the mean of the normalized decibel-scale data of the envelope image ( $E$ ) inside the target,  $\mu_{\text{out}}$  is the mean of  $E$  outside the target,  $\sigma_{\text{in}}^2$  is the variance of  $E$  inside

the target, and  $\sigma_{\text{out}}^2$  is the variance of  $E$  outside the target. The CNR was calculated by taking a square sample region inside the target and a square sample region outside the target of equal size, located at the same axial depth. For the hyperechoic target, a 6 mm  $\times$  6 mm region (corresponding to 20 by 660 samples) was used. The anechoic targets were smaller; therefore, a region of 2.5 mm  $\times$  2.5 mm (corresponding to 8 by 280 samples) was used.

In addition to the hyperechoic and anechoic targets, the phantom contained a variety of wire targets in different configurations. These wire targets were made of nylon and had a diameter of 0.12 mm. The wire targets were used to experimentally quantify the beamwidth associated with the NSI technique and assess the ability of NSI to detect small pointlike targets. The beamwidth was estimated at the  $-6$ -dB level taken from cross sections of the wire target images at the successive focal depths.

To test the influence of noise on the NSI approach, zero-mean white Gaussian noise was added to the prebeamformed RF data from the wire targets at SNRs of 35 and 10 dB. The  $\Delta$ SNR between images before and after beamforming was then calculated by subtracting the image without the added noise from the noisy image, leaving effectively an image only comprised of noise.  $\Delta$ SNR was then computed from this image as

$$\Delta\text{SNR} = 10 \log_{10}[\text{Var}(E_{\text{NOISE}}(t))] \quad (11)$$

where  $E_{\text{NOISE}}(t)$  represents the noise only image. The SNR, therefore, represents the log average of the variances of each scan line in the image. DAS beamforming using NSI and rectangular apodization was used to reconstruct the images. The SNR of the beamformed data was quantified for different levels of added noise to the prebeamformed data and compared between the apodization schemes.

Finally, the speckle statistics were quantified for NSI and compared to rectangular apodization. This calculation was performed because NSI produces images with pointlike speckle that appears underdeveloped. Specifically, the speckle SNR was calculated as [23]

$$\text{sSNR} = \frac{\langle E \rangle}{\sqrt{\langle E^2 \rangle - \langle E \rangle^2}} \quad (12)$$

where  $\langle E \rangle$  represents the spatial average of the envelope image over a defined data block in a homogeneous speckle region of width 10 mm  $\times$  10 mm. A histogram plot of the intensities in this region was also generated for rectangular apodization and NSI envelopes. A lateral speckle decorrelation length was also calculated for NSI and compared to speckle produced when using rectangular apodization. This length was calculated as the distance over which the autocorrelation of the square of the envelope image reduced to  $1/\sqrt{2}$  of the maximum correlation. The speckle decorrelation length was calculated at a depth of 20 mm in a speckle only region.

### E. PICMUS Data Set Reconstructions

NSI was also evaluated using *in vivo* scans obtained from the Plane-Wave Imaging Challenge in Medical

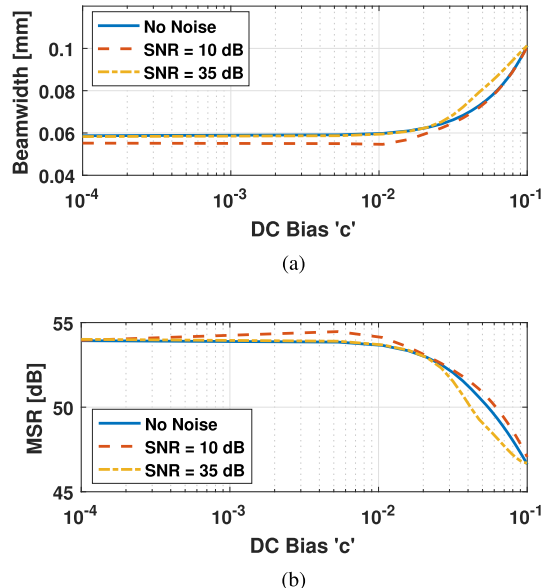


Fig. 6. Effect of dc bias on (a) beamwidth and (b) MSR.

UltraSound (PICMUS) [24]. The data set contained longitudinal and cross-sectional scans of the carotid artery. Each scan contained plane-wave data for 75 angles between  $\theta = -16^\circ$  and  $\theta = 16^\circ$ . The dc bias used here was 0.05.

To allow for a comparison of NSI against other methods, an experimental scan and a simulation scan from the PICMUS data set were chosen for beamwidth and contrast measurements, respectively. These scans were also reconstructed using all 75 angles of the plane-wave data. The dc bias used to reconstruct the experimental data was 0.01 and the dc bias used to reconstruct the simulation data was 0.05. These beamwidth and contrast measurements were made using the evaluation script provided with the PICMUS data.

## V. RESULTS

### A. Simulations

Results from the beamwidth simulations using Field II are shown in Fig. 4. The MSR values from the simulation are listed in Table I for the different apodization schemes, including two dc offsets for NSI. The MSR increased by 32.9 dB when comparing the NSI apodization ( $c = 0.05$ ) to rectangular apodization. The MSR for NSI ( $c = 0.05$ ) was less than the MSR for MV beamforming by 15.2 dB.

The beam patterns shown in Fig. 4 are all normalized to their own max, but they were also compared to each other at the same gain to observe the effect of subtracting two very similar envelopes (zero-mean envelope and the dc sum envelope). It was observed that the NSI peak was lower than the Rect peak by 32.7 dB.

The results of varying the dc bias are shown in Fig. 6 for different amounts of added noise. It was observed that as the dc bias is reduced from 0.1 to 0.01, there is a noticeable reduction in beamwidth and increase in MSR, but reducing the dc bias further below 0.01 did not have much of an impact.

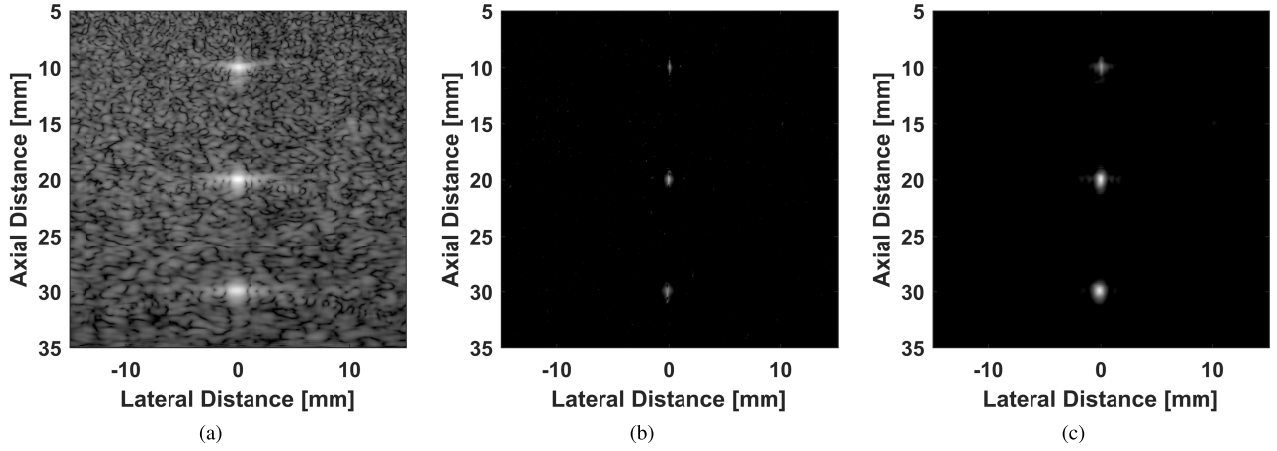


Fig. 7. Images of the AT539 phantom's wire targets. (a) Rectangular apodization. (b) NSI ( $c = 0.01$ ). (c) MV. Dynamic range is 60 dB.

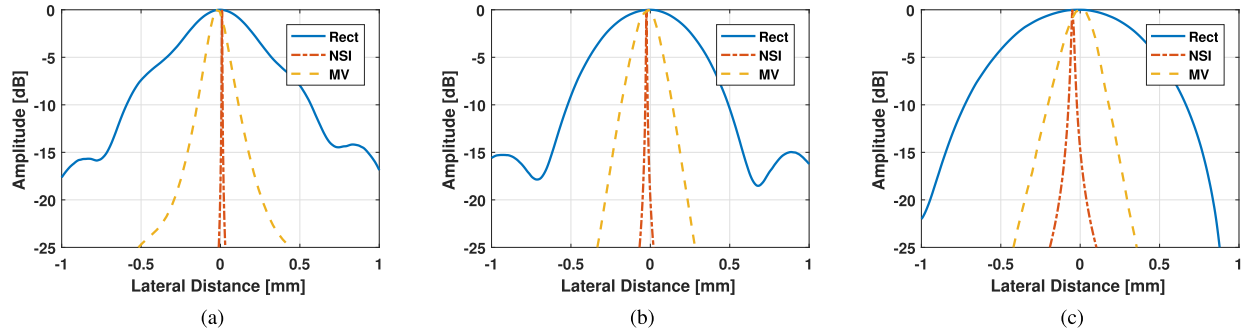


Fig. 8. Lateral cross sections of the AT539 phantom's wire targets. (a) 1-cm depth, (b) 2-cm depth, and (c) 3-cm depth.

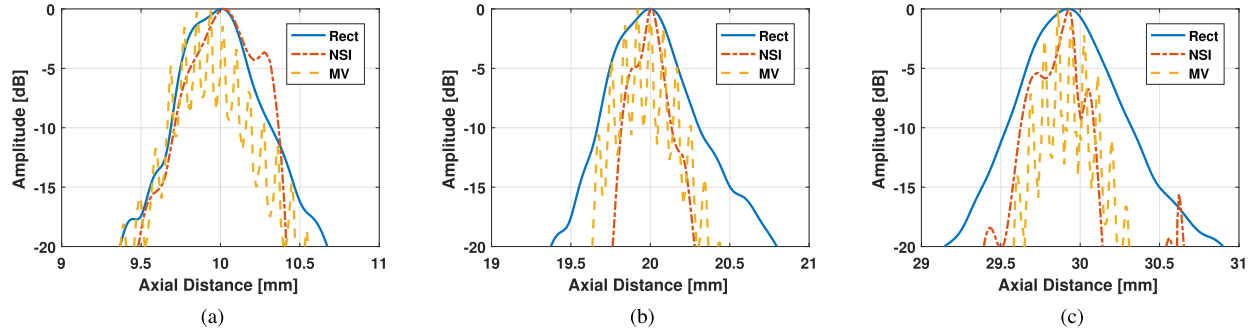


Fig. 9. Axial cross sections of the AT539 phantom's wire targets. (a) 1-cm depth, (b) 2-cm depth, and (c) 3-cm depth.

### B. Wire Targets

Results from the wire targets in the AT5 phantom experiments are shown in Figs. 7–9 and Table II. Specifically, images of the wire targets are shown in Fig. 7, lateral and axial cross sections are shown in Figs. 8 and 9, and associated metrics from cross sections are provided in Table II. The cross sections show that only the lateral point spread function (PSF) changes with NSI; the axial PSF does not change. The beamwidths that were calculated from the different wire targets under the different NSI apodization schemes provided improvement over the diffraction-limited rectangular apodization and the MV beamforming method. The beamforming aperture used was 9.75 mm, and the targets were located at depths of 1, 2, and 3 cm, respectively.

The beamforming aperture was chosen such that the  $f/\#$ s at each target depth would approximately be equal to 1, 2, and 3, respectively. In Table II(b), the measured beamwidth values are shown in terms of the wavelength of the center frequency of the pulse.

At  $-6$  dB, the theoretical predicted beamwidth values for an unapodized aperture were calculated according to  $D_f = 1.41\lambda f^\#$ . The wavelength of the pulse used for imaging was 0.31 mm. Thus, for rectangular apodization, the beamwidths measured for the 2- and 3-cm targets were close to theoretical values (0.872 and 1.311 mm, respectively); however, the 1-cm target was much larger than the theoretical value (0.44 mm). The theoretical beamwidth values for NSI were calculated according to (9). Ignoring the element

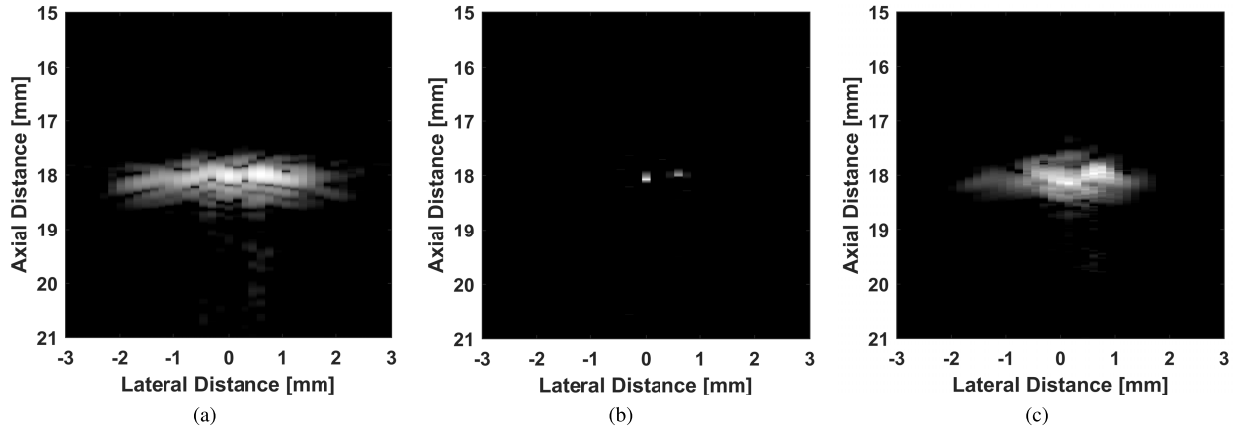


Fig. 10. Images of two closely ( $<1$  mm) spaced wire targets. (a) Rectangular apodization. (b) NSI ( $c = 0.01$ ). (c) MV. Dynamic Range is 40 dB.

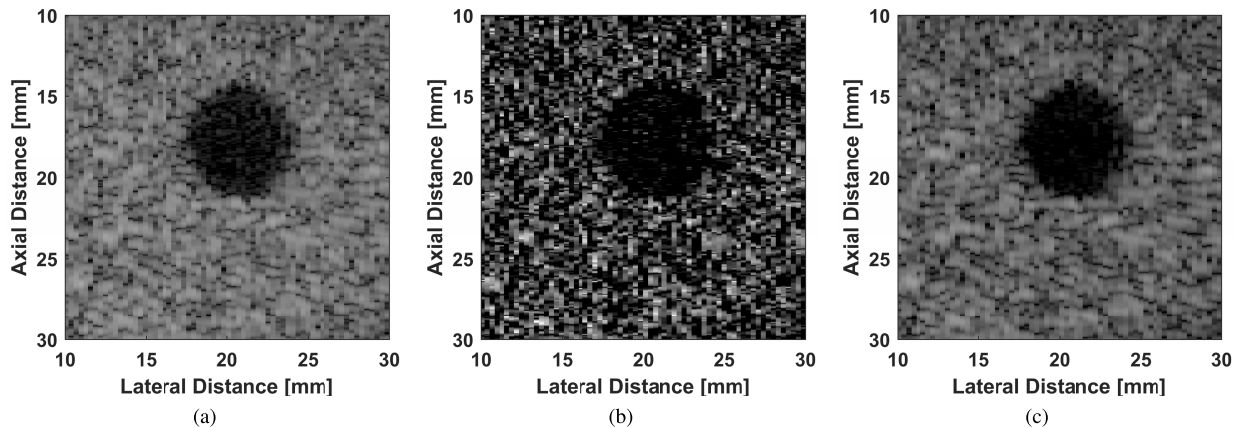


Fig. 11. Images of the ATS539 phantom's anechoic targets. (a) Rectangular apodization. (b) NSI ( $c = 0.05$ ). (c) MV. Dynamic range is 60 dB.

TABLE II

COMPARISON OF THE LATERAL SPREAD OF WIRE TARGETS ( $-6$  dB) AT SUCCESSIVE DEPTHS. (a) BEAMWIDTH (mm). (b) BEAMWIDTH ( $\lambda$ )

Depth (cm)	Rect	NSI ( $c = 0.01$ )	NSI ( $c = 0.1$ )	MV
1	0.79	0.005	0.04	0.18
2	0.81	0.008	0.06	0.23
3	1.12	0.031	0.15	0.28

(a)

Depth (cm)	Rect	NSI ( $c = 0.01$ )	NSI ( $c = 0.1$ )	MV
1	2.74	0.02	0.13	0.61
2	2.79	0.03	0.19	0.81
3	3.88	0.10	0.49	0.95

(b)

factor and using a pitch ( $d = 0.3048 \mu\text{m}$ ) corresponding to the L9-4 array and a center frequency of 5 MHz provides an opening angle corresponding to the  $-6$ -dB beamwidth of  $0.0435^\circ$ , which provides a beamwidth of  $15 \mu\text{m}$  at 1-cm depth or  $30 \mu\text{m}$  at 2-cm depth. However, the beamwidths measured from the ATS phantom data were lower, i.e., 5 and  $8 \mu\text{m}$  at 1- and 2-cm depths, respectively.

In the case of the NSI apodization scheme where  $c = 0.01$ , for the 2-cm target, the beamwidth measured at  $-6$  dB was narrower by a factor of approximately 100 compared to rectangular apodization, i.e., the diffraction limited case. The worst case improvement in resolution among the three wire targets was  $35\times$  (for the 3-cm target with  $c = 0.01$ ).

As a further test of spatial resolution afforded by the NSI approach, two wire targets spaced close together were imaged using rectangular apodization and NSI ( $c = 0.01$ ). The images of the two wire targets are shown in Fig. 10, with a 40-dB dynamic range for better visualization. The images indicate that the NSI method was able to distinguish between the two wires, whereas the rectangular apodization image showed the two wires smeared together. In bringing the wires closer together, we observed a flat top, i.e., the Sparrow criterion, for the rectangular apodized images, but were unable to achieve a Sparrow-like condition for NSI. The images went from separable wire targets to a single smeared out point with NSI as the wire was drawn closer together.

### C. Cyst Phantom

The images from anechoic targets are shown in Fig. 11 and the CNR values are listed in Table III for the different apodization schemes. When examining anechoic targets,

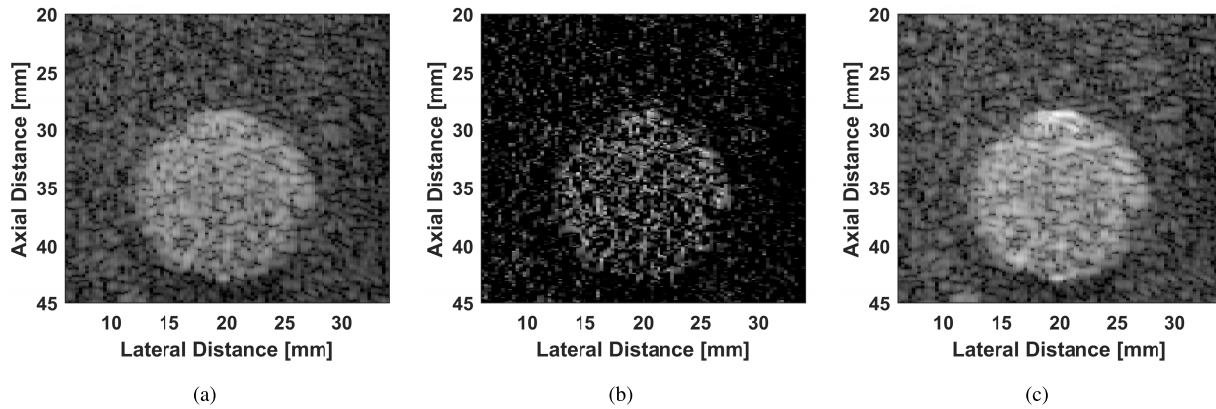


Fig. 12. Images of the AT539 phantom's hyperechoic targets. (a) Rectangular apodization. (b) NSI ( $c = 0.05$ ). (c) MV. Dynamic range is 60 dB.

TABLE III  
COMPARISON OF CNR IN CONTRAST TARGETS

Target	Rect	NSI	MV
Anechoic	-3.05	-1.01	-3.27
Hyperechoic	1.65	0.45	1.89

the magnitude of the CNR was observed to decrease for NSI compared to rectangular apodization and MV beamforming. For the anechoic targets (Fig. 11), a CNR of  $-1.01$  was obtained using NSI, while using a rectangular apodization and MV beamforming yielded a CNR of  $-3.05$  and  $-3.27$ , respectively. Therefore, based on the CNR metric, the NSI scheme greatly reduced the ability to detect anechoic targets.

As in the case of anechoic targets, NSI performed worse than rectangular apodization and the MV beamformer when tasked with detecting and imaging hyperechoic targets. Fig. 12 shows the images of hyperechoic targets when using the different apodization schemes. The associated CNR values are listed in Table III. CNR values for rectangular apodization, NSI, and MV beamforming were 1.65, 0.45, and 1.89, respectively.

The reduction of CNR magnitude for both the anechoic and hyperechoic targets when using NSI is related to the change in the speckle characteristics that occur due to the nonlinear processing of the images. To quantify this speckle, the sSNR was calculated for images created using NSI and rectangular apodization in speckle-only regions. An average sSNR of 1.62 was observed for the rectangular apodization, while an average sSNR of 0.51 was observed for NSI. This indicates that for NSI, the speckle was no longer fully developed, i.e., fully developed speckle has an sSNR close to 1.91. Fig. 13 provides a graph of the speckle decorrelation curves produced when using NSI versus rectangular apodization. As is apparent, the NSI curve produced speckle that decorrelated rapidly versus lateral distance. The distance at which the speckle decorrelated to  $1/\sqrt{2}$  of its maximum correlation in millimeters was 0.012 and 0.255 mm for NSI and rectangular apodization, respectively.

The CNR metric decreased as the variance of the speckle increased. In the case of the NSI image, speckle varies greatly because of the nonlinear processing scheme and the small resolution cell size. This causes the speckle to be underdeveloped,

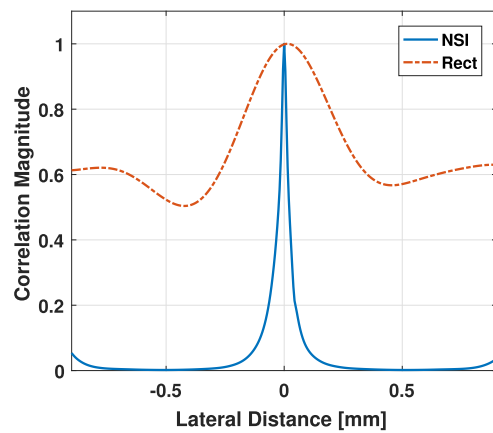


Fig. 13. Lateral autocorrelation of the speckle envelope images produced using NSI and rectangular apodization.

TABLE IV  
COMPARISON OF SNR OF PREBEAMFORMED DATA VERSUS POSTBEAMFORMED DATA

Pre-Beamformed	Rect	NSI
35 dB	44 dB	51 dB
10 dB	21 dB	37 dB

thus decreasing the ability to see contrast between the background speckle and either an anechoic or hyperechoic target. On the other hand, the image constructed using rectangular apodization has fully developed speckle in and around the contrast targets resulting in lower variance in the intensity of the image, and thus higher CNR.

The influence of electronic noise on the ability of NSI to produce images was also assessed. Fig. 14 shows the images of the cross section across the wire targets for different levels of noise added to the prebeamformed data. Table IV provides the SNRs in the NSI and rectangular images for different levels of prebeamformed noise.

#### D. PICMUS Data Set

The images reconstructed from the PICMUS data set are shown in Fig. 15. The *in vivo* reconstructions are shown

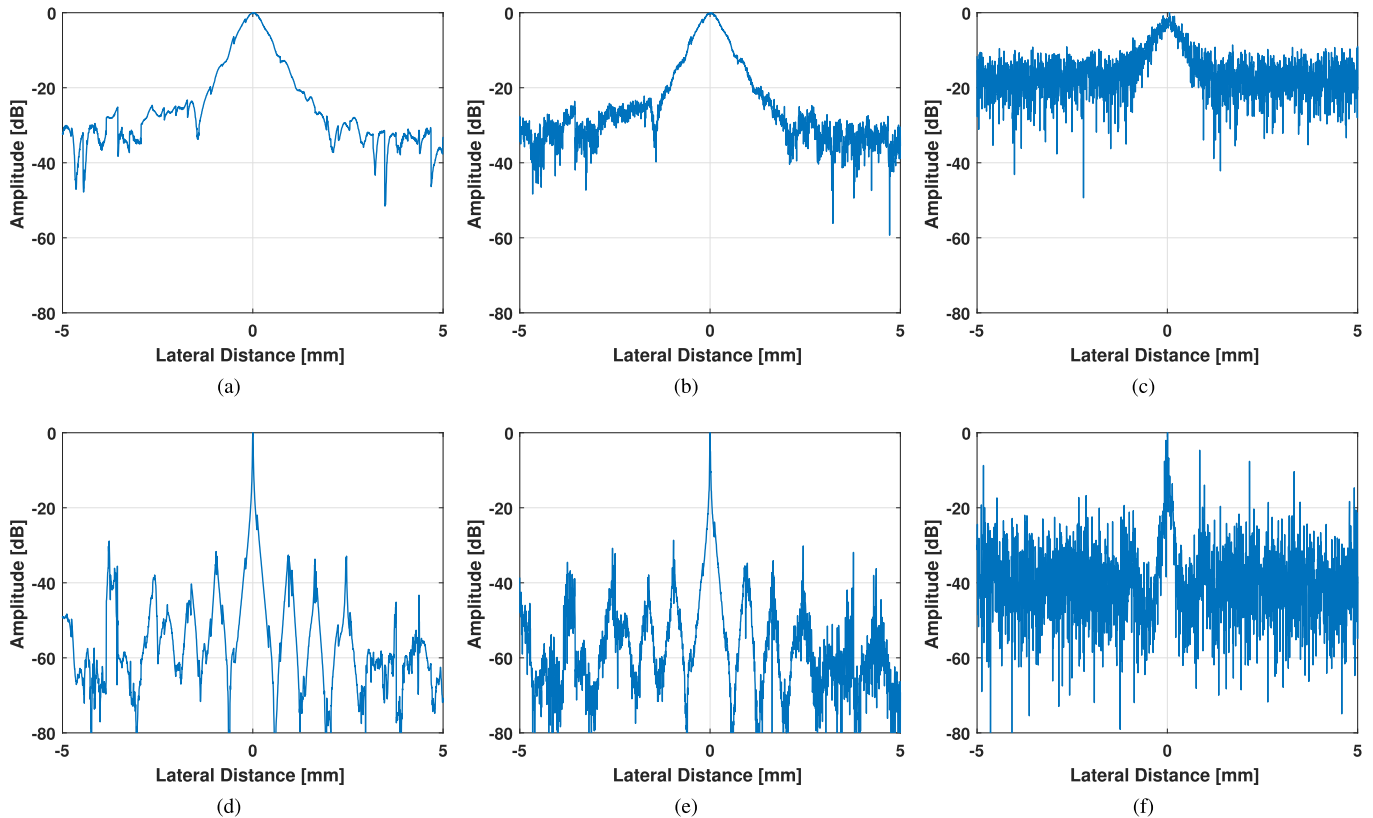


Fig. 14. Cross sections of the ATSS539 phantom's 1-cm-depth wire target without and with white Gaussian noise added prior to beamforming. (a) Rectangular apodization, no noise added. (b) Rectangular Apodization, prebeamformed SNR = 35 dB. (c) Rectangular apodization, prebeamformed SNR = 10 dB. (d) NSI, no noise added. (e) NSI, prebeamformed SNR = 35 dB. (f) NSI, prebeamformed SNR = 10 dB.

in Fig. 15(a), (b), (d), and (e). Similar to the ATS phantom results, the contrast with NSI is lower than rectangular apodization. Fig. 15(c) shows the reconstructed simulation data for contrast measurements. The mean contrast was measured to be 3.77 dB. Fig. 15(f) shows the reconstructed experimental data for resolution measurements. The mean lateral resolution was measured to be 0.09 mm. Comparing NSI results with the  $l1$ -norm-based beamforming method presented in [25] indicates that NSI had worse mean contrast than the  $l1$ -norm-based method, but comparable mean beamwidth.

## VI. DISCUSSION

A novel apodization scheme, NSI, was evaluated for engaging in specific imaging tasks: detection of pointlike targets, detection of anechoic targets, and detection of hyperechoic targets. The NSI imaging technique takes advantage of the sharp rolloff of nulls in the beam pattern to produce images that have dramatically improved lateral resolution while still maintaining the low sidelobe levels. To achieve these improvements in lateral resolution requires subtraction of envelope-based images, which results in a nonlinear image processing scheme.

Based on the images produced by NSI for specific imaging tasks, several important observations can be made. First, when imaging wire targets, NSI was able to produce images with very high lateral resolution, i.e., more than  $35\times$  better than rectangular apodization (the diffraction limit). At the same

time, this improvement in lateral resolution was also associated with a decrease in the sidelobe levels of the beam as evidenced by the increased estimates of MSR. Furthermore, in Fig. 7, the NSI approach appeared to suppress speckle surrounding the small bright targets in the field, making these targets stand out more than with rectangular apodization.

Compared to MV beamforming, NSI produced images with lateral resolution improved by a factor of 2–4 (depth dependent). The advantage of using NSI over MV beamforming is that NSI is computationally less expensive because it uses only three apodizations that are data independent.

The wire target images suggest that an imaging mode using NSI could perform better at detecting small specular targets in the field more than traditional apodization approaches. In this regard, applications for NSI could include the detection of microcalcifications. Microcalcifications are small deposits of calcium in the body that typically form in clumps. The presence of microcalcifications in breast tissue or thyroid is an important indicator of cancerous tissue; however, medical ultrasound currently has a limited role in their detection [26]. This is because microcalcifications, while highly reflective, are small compared to the beamwidth of ultrasound and are, thus, not easily distinguished from each other. To test the ability of NSI to distinguish multiple closely spaced targets, images were taken of two wires spaced less than 1 mm apart laterally (displayed in Fig. 10). NSI was able to clearly differentiate the two wire targets, whereas rectangular apodization could not.

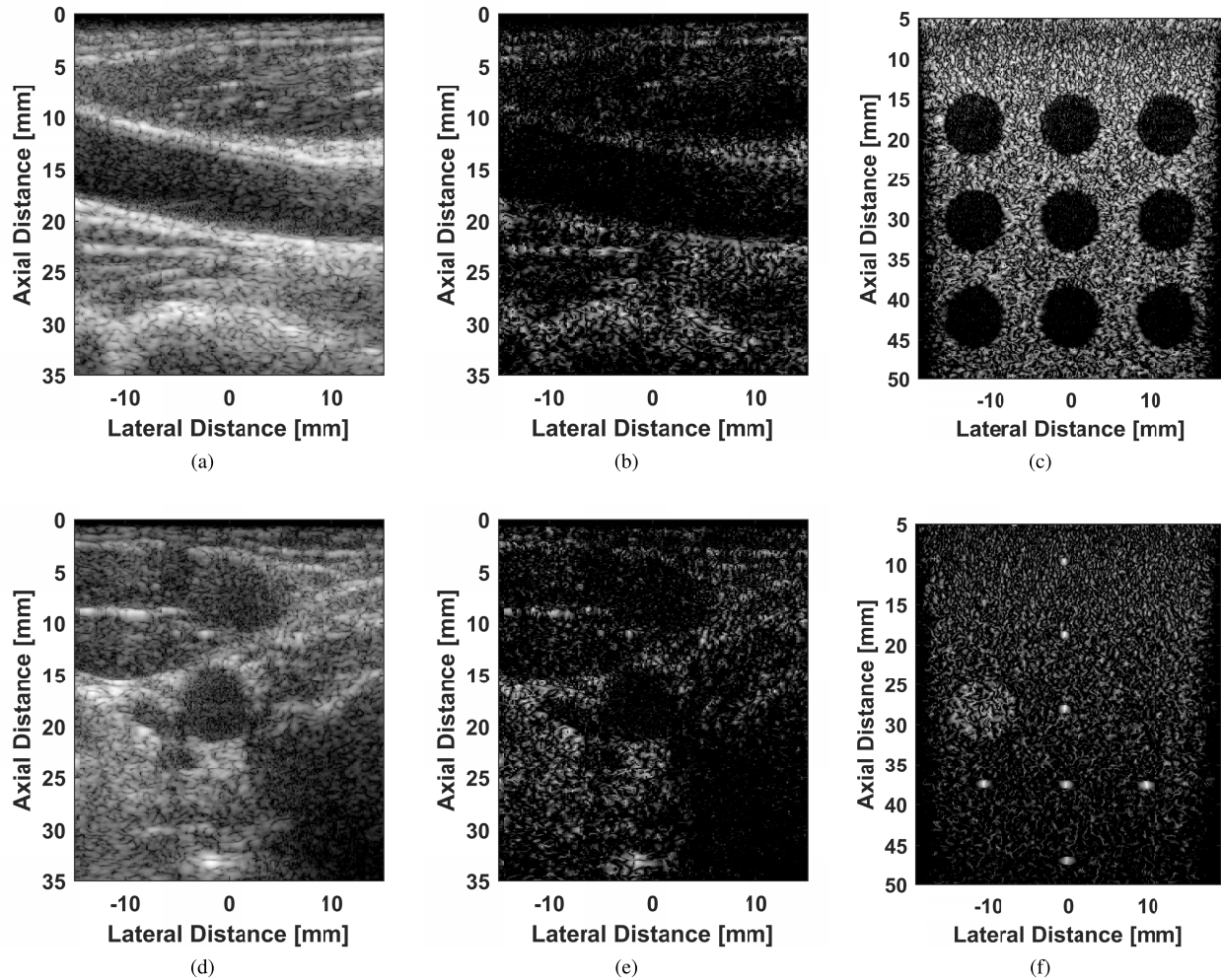


Fig. 15. Images reconstructed from the PICMUS data set. (a) and (b) Longitudinal section of the carotid artery. (d) and (e) Cross section of the carotid artery. (c) Simulation (Contrast). (f) Experiment (resolution). (a) and (d) Rectangular apodization. (b), (c), and (e) NSI ( $c = 0.05$ ). (f) NSI ( $c = 0.01$ ). Dynamic range is 60 dB.

For the specific task of imaging anechoic targets, NSI did not perform well compared to rectangular apodization. The CNR decreased dramatically for the NSI images compared to rectangular apodization, i.e.,  $-3.05$  to  $-1.01$ . This decrease in the CNR is due to the changes that occurred in the speckle characteristics of the NSI images. Specifically, while the images produced using rectangular apodization had close to fully developed speckle, the NSI images did not have fully developed speckle.

The speckle in the NSI images was characterized by very small bright speckle spots with a very narrow speckle decorrelation length. Part of the shrinking of the speckle size may be due to the narrowness of the NSI beam and part of the speckle size reduction is due to the nonlinear processing of the images with NSI. With the shrinking of the resolution cell, the number of scatterers per resolution cell would be reduced, which reduces the intensity of the image speckle linearly with the number of scatterers per resolution cell [27]–[29]. The histogram plots in Fig. 16 showing the effect of reduced scatterer density with NSI match the results in [30]. For the wire target located at 2-cm depth, the apparent

lateral resolution was decreased by a factor of 100 when using NSI compared to rectangular apodization, suggesting the speckle intensity should decrease by  $10 \log_{10}(100^2) = 40.0$  dB. The factor of 100 is squared because the resolution cell is proportional to the lateral beamwidth squared. Comparing the speckle-only intensity, i.e., outside of the wire target, of the NSI image and the rectangular apodization image at the depth of 2 cm gave values of  $-77.6$  and  $-29.1$  dB for NSI and rectangular apodizations, respectively. This is close to the 40-dB reduction in speckle intensity that would be predicted by the reduction in the resolution cell size due to narrowing of the lateral beamwidth. Simulation experiments with varying scatterer density revealed that the intensity does increase as the scatterer density is increased, but the sSNR never approaches 1.91 with NSI as the scatterer number density increased. This would indicate that NSI does not produce fully developed speckle under that same conditions as conventional beamforming. The reasons for this are currently unknown.

As a result of the changes in the speckle, the intensity variations of the images were much higher and the background

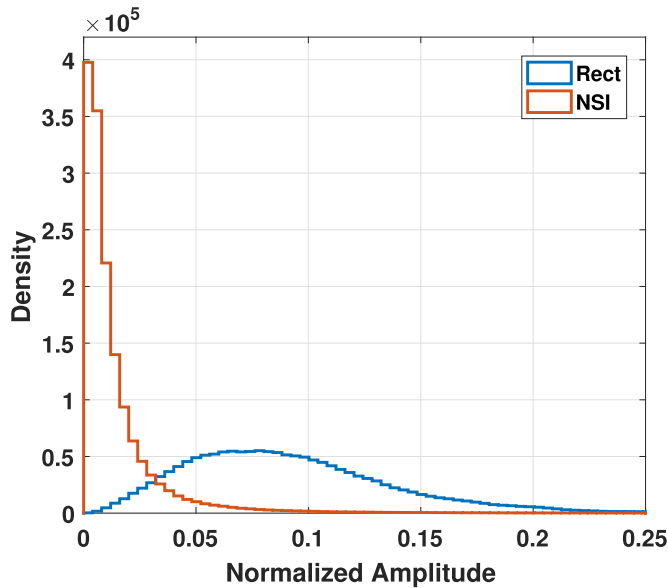


Fig. 16. Histogram plots of the envelope amplitudes for rectangular apodization and NSI.

of the images was characterized by larger regions of dark space between the speckle bright spots. This reduced the ability to detect the anechoic and hyperechoic targets. Furthermore, in the wire target images, the speckle was suppressed compared to the bright specular wire targets because a narrowing of the NSI beam would not affect the intensity from the specular scatterer in the same way that the speckle intensity is reduced. This again would suggest that a good application for NSI is detecting small specular targets in a speckle background, like microcalcifications, by NSI's suppression of speckle around small specular scatterers. In addition, the narrow speckle decorrelation length of NSI images suggests that another task for which NSI may be well suited is tracking of speckle in the lateral direction.

The third imaging task was to evaluate NSI for the detection of hyperechoic targets. Similar to the anechoic target detection, NSI provided much lower CNR than rectangular apodization. Again, the loss in CNR for NSI was due to the speckle characteristics, which did not have fully developed speckle.

The robustness of NSI in the presence of noise was also evaluated. The SNR of NSI was observed to increase over rectangular apodization. Improvements in SNR of 16 dB were observed with NSI after beamforming. These increases in SNR are attributable to the process of image formation using NSI where highly correlated signals are subtracted from one another. The subtraction results in a cancelation of much of the noise present in the signals. For the additive white Gaussian noise applied to the prebeamformed data, noise distorted the shape of the main lobe but did not significantly impact the overall  $-6$ -dB beamwidth. It was also observed that as SNR decreased in the prebeamformed data, targets and sidelobes became more easily indistinguishable from the noise as depth increased. This was observed when the prebeamformed SNR was 10 dB. The wire target located at 3-cm depth disappeared in the noise for all imaging schemes.

## VII. CONCLUSION

With NSI, a factor of improvement in the apparent lateral resolution of at least  $10\times$  compared to the rectangular apodization was achieved. In experiments, improvements in the apparent lateral resolution of more than  $35\times$  were observed with NSI compared to rectangular apodization. Improvement in sidelobes by an average of 32 dB over the rectangular apodization was also observed when using NSI. For contrast targets, a decrease in CNR was observed using NSI that could not fully be compensated. The results show that NSI may be well suited for the detection of small, highly reflective targets, and despite the lower CNR, NSI is still able to differentiate anechoic and hyperechoic targets from the background. As NSI is implemented passively on receive, one can easily switch between the rectangular apodization and NSI depending on the situation.

There is still much work to be done with NSI. Two related problems are the contrast and the speckle. The speckle statistics could not be explained completely, and therefore, it is still not well understood why the speckle does not fully develop in an image. Understanding this could lead to improving contrast in NSI images.

## ACKNOWLEDGMENT

The content is solely the responsibility of the authors and does not necessarily represent the official views of the National Institutes of Health. The authors would like to thank R. J. Miller and T. N. Nguyen for their assistance in collecting data for this work.

## REFERENCES

- [1] F. J. Harris, "On the use of windows for harmonic analysis with the discrete Fourier transform," *Proc. IEEE*, vol. 66, no. 1, pp. 51–83, Jan. 1978.
- [2] C. L. Dolph, "A current distribution for broadside arrays which optimizes the relationship between beam width and side-lobe level," *Proc. IRE*, vol. 34, no. 6, pp. 335–348, Jun. 1946.
- [3] T. T. Taylor, "Design of line-source antennas for narrow beamwidth and low sidelobes," *IRE Trans. Antennas Propag.*, vol. AP-3, no. 1, pp. 16–28, Jan. 1955.
- [4] P. Hoen, "Aperture apodization to reduce the off-axis intensity of the pulsed-mode directivity function of linear arrays," *Ultrasonics*, vol. 20, no. 5, pp. 231–236, Sep. 1982.
- [5] D. A. Guenther and W. F. Walker, "Optimal apodization design for medical ultrasound using constrained least squares part I: Theory," *IEEE Trans. Ultrason., Ferroelectr., Freq. Control*, vol. 54, no. 2, pp. 332–342, Feb. 2007.
- [6] D. A. Guenther and W. F. Walker, "Optimal apodization design for medical ultrasound using constrained least squares part II simulation results," *IEEE Trans. Ultrason., Ferroelectr., Freq. Control*, vol. 54, no. 2, pp. 343–358, Feb. 2007.
- [7] C. H. Seo and J. T. Yen, "Sidelobe suppression in ultrasound imaging using dual apodization with cross-correlation," *IEEE Trans. Ultrason., Ferroelectr., Freq. Control*, vol. 55, no. 10, pp. 2198–2210, Oct. 2008.
- [8] H. Wang, "System and method for adaptive beamformer apodization," U.S. Patent 6436044 B1, Aug. 20, 2002.
- [9] J. Guo, L. Chen, Y. Zhang, K. Yang, J. Li, and X. Gao, "Method of ultrasonic phased array imaging based on segment amplitude apodization," in *Proc. Far East Forum Nondestruct. Eval./Testing, New Technol. Appl.*, Jun. 2013, pp. 181–188.
- [10] J. H. Sung and J. S. Jeong, "Dual-/tri-apodization techniques for high frequency ultrasound imaging: A simulation study," *Biomed. Eng. OnLine*, vol. 13, no. 1, p. 143, 2014.
- [11] Z. He, F. Zheng, Y. Ma, H. H. Kim, Q. Zhou, and K. K. Shung, "A sidelobe suppressing near-field beamforming approach for ultrasound array imaging," *J. Acoust. Soc. Amer.*, vol. 137, no. 5, pp. 2785–2790, May 2015.

- [12] F. Viola and W. F. Walker, "Adaptive signal processing in medical ultrasound beamforming," in *Proc. IEEE Ultrason. Symp.*, vol. 4, Sep. 2005, pp. 1980–1983.
- [13] I. K. Holfort, F. Gran, and J. A. Jensen, "Broadband minimum variance beamforming for ultrasound imaging," *IEEE Trans. Ultrason., Ferroelectr., Freq. Control*, vol. 56, no. 2, pp. 314–325, Feb. 2009.
- [14] J. F. Synnevåg, C. I. C. Nilsen, and S. Holm, "P2B-13 speckle statistics in adaptive beamforming," in *Proc. IEEE Ultrason. Symp.*, Oct. 2007, pp. 1545–1548.
- [15] J.-F. Synnevåg, A. Austeng, and S. Holm, "A low-complexity data-dependent beamformer," *IEEE Trans. Ultrason., Ferroelectr., Freq. Control*, vol. 58, no. 2, pp. 281–289, Feb. 2011.
- [16] A. C. Jensen and A. Austeng, "An approach to multibeam covariance matrices for adaptive beamforming in ultrasonography," *IEEE Trans. Ultrason., Ferroelectr., Freq. Control*, vol. 59, no. 6, pp. 1139–1148, Jun. 2012.
- [17] A. C. Jensen and A. Austeng, "The iterative adaptive approach in medical ultrasound imaging," *IEEE Trans. Ultrason., Ferroelectr., Freq. Control*, vol. 61, no. 10, pp. 1688–1697, Oct. 2014.
- [18] R. Cobbold, *Foundations of Biomedical Ultrasound* (Biomedical Engineering Series). London, U.K.: Oxford Univ. Press, 2007.
- [19] A. S. Savoia *et al.*, "Improved lateral resolution and contrast in ultrasound imaging using a sidelobe masking technique," in *Proc. IEEE Int. Ultrason. Symp.*, Sep. 2014, pp. 1682–1685.
- [20] J. A. Jensen, "FIELD: A program for simulating ultrasound systems," in *Proc. IEEE 10th Nordic-Baltic Conf. Biomed. Imag.*, vol. 34, Mar. 1996, pp. 351–353.
- [21] J. A. Jensen and N. B. Svendsen, "Calculation of pressure fields from arbitrarily shaped, apodized, and excited ultrasound transducers," *IEEE Trans. Ultrason., Ferroelectr., Freq. Control*, vol. 39, no. 2, pp. 262–267, Mar. 1992.
- [22] J.-F. Synnevåg, A. Austeng, and S. Holm, "Benefits of minimum-variance beamforming in medical ultrasound imaging," *IEEE Trans. Ultrason., Ferroelectr., Freq. Control*, vol. 56, no. 9, pp. 1868–1879, Sep. 2009.
- [23] C. B. Burckhardt, "Speckle in ultrasound B-mode scans," *IEEE Trans. Sonics Ultrason.*, vol. SU-25, no. 1, pp. 1–6, Jan. 1978.
- [24] H. Liebgott, A. Rodriguez-Molares, F. Cervenansky, J. A. Jensen, and O. Bernard, "Plane-wave imaging challenge in medical ultrasound," in *Proc. IEEE Ultrason. Symp.*, Sep. 2016, pp. 1–4.
- [25] T. Szasz, A. Basarab, and D. Kouamé, " $l_1$ -norm regularized beamforming in ultrasound imaging," in *Proc. IEEE Int. Ultrason. Symp. (IUS)*, Sep. 2016, pp. 1–3.
- [26] P. Machado, J. R. Eisenbrey, B. Cavanaugh, and F. Forsberg, "New image processing technique for evaluating breast microcalcifications, a comparative study," *J. Ultrasound Med.*, vol. 31, no. 6, pp. 885–893, Jun. 2012.
- [27] M. F. Insana, J. A. Zagzebski, and E. L. Madsen, "Acoustic back scattering from ultrasonically tissue-like media," *Med. Phys.*, vol. 9, no. 6, pp. 848–855, 1982.
- [28] S. Smith, H. Lopez, and W. Bodine, "Frequency independent ultrasound contrast-detail analysis," *Ultrasound Med. Biol.*, vol. 11, no. 3, pp. 467–477, May 1985.
- [29] B. J. Oosterveld, J. M. Thijssen, and W. A. Verhoef, "Texture of B-mode echograms: 3-D simulations and experiments of the effects of diffraction and scatterer density," *Ultrason. Imag.*, vol. 7, no. 2, pp. 142–160, 1985.
- [30] X. Hu, Y. Zhang, L. Deng, S. Peng, and K. Zhang, "A comparison of the Homodyned K-distribution and the single distributions for RF ultrasonic speckle modeling," in *Proc. BMEI*, Oct. 2015, pp. 131–136.



**Anil Agarwal** (S'12–GS'17) received the B.S. degree in electrical engineering from the University of Illinois at Urbana–Champaign, Urbana, IL, USA, in 2016, where he is currently pursuing the M.S. degree in electrical and computer engineering.

His research interests include digital signal processing, acoustics, biomedical image processing, and ultrasound beamforming.



**Jonathan Reeg** (S'11–GS'15–M'16) received the B.S. degree in electrical engineering and the M.S. degree in electrical and computer engineering from the University of Illinois at Urbana–Champaign, Urbana, IL, USA, in 2014 and 2016, respectively.

He is currently an Electroacoustic Engineer with Knowles Corporation, Itasca, IL, USA, where he is involved in the design of MEMS microphones for use in consumer electronics. His research interests while at the University of Illinois at Urbana–Champaign included quantitative ultrasound imaging and beamformation.

**Anthony S. Podkova** (GS'14) received dual B.S. degrees in physics and electrical and computer engineering (ECE) from Bradley University, Peoria, IL, USA, in 2013, and the M.S. degree in ECE from the University of Illinois at Urbana–Champaign, Urbana, IL, USA, in 2017, where he is currently pursuing the Ph.D. degree in ECE, with a focus on quantitative biomedical ultrasonic imaging.

His research interests include ultrasonic computed tomography, inverse problems, beamformation, pulse compression, color flow Doppler imaging, and multirate signal processing.



**Michael L. Oelze** (M'03–SM'09) was born in Hamilton, New Zealand, in 1971. He received the B.S. degree in physics and mathematics from Harding University, Searcy, AR, USA, in 1994, and the Ph.D. degree in physics from the University of Mississippi, Oxford, MS, USA.

From 2000 to 2002, he was a Post-Doctoral Researcher with the Bioacoustics Research Laboratory, Department of Electrical and Computer Engineering (ECE), University of Illinois at Urbana–Champaign (UIUC), Urbana, IL, USA. From 2002 to 2004, he was an NIH Fellow conducting research in quantitative ultrasound techniques for biomedical ultrasound applications in cancer detection. In 2005, he joined the Faculty of ECE, UIUC, where he is currently a Professor and the Associate Head for Graduate Affairs. His research interests include biomedical ultrasound, quantitative ultrasound imaging for improving cancer diagnostics and monitoring therapy response, ultrasound bioeffects, ultrasound tomography techniques, ultrasound-based therapy, beamforming, and applications of coded excitation to ultrasonic imaging.

Dr. Oelze is currently a Fellow of the AIUM, and a member of ASA. He is a member of the Technical Program Committee of the IEEE Ultrasonics Symposium. He currently serves as an Associate Editor of IEEE TRANSACTIONS ON ULTRASONICS, FERROELECTRICS, AND FREQUENCY CONTROL, *Ultrasonic Imaging*, and IEEE TRANSACTIONS ON BIOMEDICAL ENGINEERING.